

Distribution of primary and secondary features in the Pahrump Hills outcrop (Gale crater, Mars) as seen in a Mars Descent Imager (MARDI) “sidewalk” mosaic



Michelle E. Minitti^{a,*}, Michael C. Malin^b, Jason K. Van Beek^b, Michael Caplinger^b, Justin N. Maki^c, Michael Ravine^b, Fred J. Calef III^c, Lauren A. Edgar^d, David Harker^b, Kenneth E. Herkenhoff^d, Linda C. Kah^e, Megan R. Kennedy^b, Gillian M. Krezoski^b, Rachel E. Kronyak^e, Leslie Lipkaman^b, Brian Nixon^b, Scott K. Rowland^f, Juergen Schieber^g, Jeffrey F. Schroeder^c, Kathryn M. Stack^c, Rebecca M.E. Williams^h, R. Aileen Yingst^h

^a Framework, 418 Hillsboro Drive, Silver Spring, MD 20902, USA

^b Malin Space Science Systems, 5880 Pacific Center Boulevard, San Diego, CA 92121, USA

^c Jet Propulsion Laboratory, California Institute of Technology, 4800 Oak Grove Drive, Pasadena, CA 91109, USA

^d United States Geological Survey, Astrogeology Science Center, 2255 N. Gemini Dr., Flagstaff, AZ 86001, USA

^e Department of Earth and Planetary Sciences, University of Tennessee, Knoxville, TN 37996-1410, USA

^f School of Ocean and Earth Science and Technology, University of Hawaii at Mānoa, Honolulu, HI 96822, USA

^g Department of Geological Sciences, Indiana University, 1001 East 10th Street, Bloomington, IN 47405-1405, USA

^h Planetary Science Institute, 1700 East Fort Lowell Road #106, Tucson, AZ 85719, USA

ARTICLE INFO

Keywords:

Mars
Mars, surface
Geological processes

ABSTRACT

The Mars Science Laboratory *Curiosity* rover conducted a reconnaissance traverse across the Pahrump Hills outcrop within Gale crater from Sols 780–797. During the traverse, the Mars Descent Imager (MARDI) acquired a continuous imaging record of primary and secondary sedimentary features throughout the outcrop. The characteristics of the features (laminae, resistant features, fractures, gray clasts) and their spatial distribution provide insight into the processes that contributed to the formation of Pahrump Hills. Thin, regular laminae (mm-scale) are ubiquitous in the bedrock, implying that depositional processes at that scale did not change appreciably during deposition of the mudstone succession at Pahrump Hills. Higher bedrock slopes correlate with undulatory bedrock surfaces, bedrock with elevated Mg contents, and fractures exhibiting wide, raised edges. These collective features are consistent with increased erosional resistance caused by greater quantities of erosion-resistant, Mg-bearing cement within the bedrock permitted by coarser grain sizes. Resistant features exhibit a range of morphologies, elevated Mg contents, and do not deflect laminae within the bedrock. Their characteristics implicate the involvement of Mg-enriched fluids in a late diagenetic overprint affecting the bedrock. The variations of fracture fill and edge morphologies and chemistries further suggest repeated fracturing and fluid interaction events within the strata exposed at Pahrump Hills. Gray clasts strongly resemble fragments eroded from sandstone horizons interspersed throughout the Pahrump Hills outcrop.

1. Introduction

With her arrival at the base of the “Pahrump Hills” outcrop on Sol 753, the Mars Science Laboratory (MSL) *Curiosity* rover began exploration of the foothills of Aeolis Mons (informally known as “Mt. Sharp”; Fig. 1). The physical and mineralogical stratigraphy of Mt. Sharp (e.g., Anderson and Bell III, 2010; Milliken et al., 2010; Thomson

et al., 2011) was the motivation for the selection of Gale crater as the landing site for MSL, a mission aimed at finding and characterizing habitable environments on Mars (Grotzinger et al., 2012). The Pahrump Hills outcrop exposes ~13 m of vertical section, and forms the lowest exposure of the Murray formation. In turn, the Murray formation itself represents the lowest exposed interval of strata associated with Mt. Sharp. After acquiring a baseline drill sample from the base of the

* Corresponding author.

E-mail address: minitti@me.com (M.E. Minitti).

<https://doi.org/10.1016/j.icarus.2019.03.005>

Received 24 October 2018; Received in revised form 1 March 2019; Accepted 6 March 2019

Available online 14 March 2019

0019-1035/ © 2019 The Authors. Published by Elsevier Inc. This is an open access article under the CC BY-NC-ND license (<http://creativecommons.org/licenses/by-nc-nd/4.0/>).

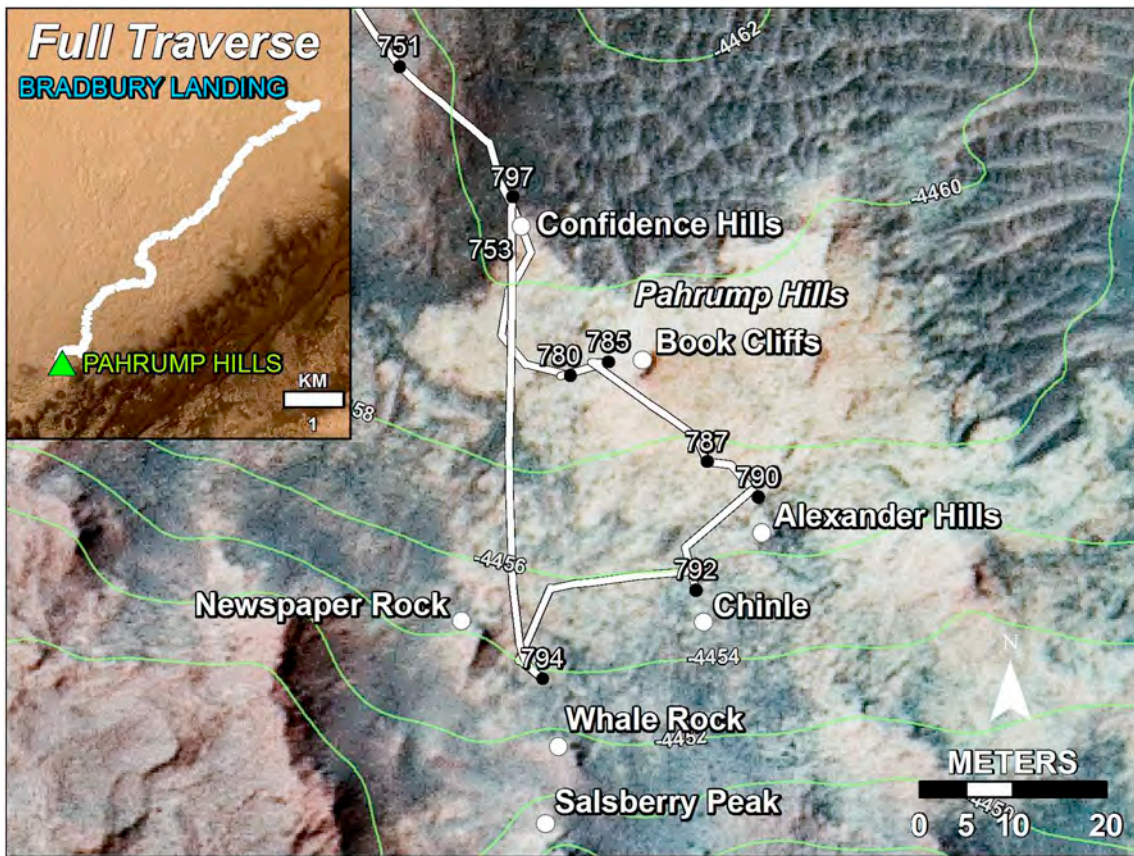


Fig. 1. Reconnaissance traverse (white line) across the Pahrump Hills outcrop overlaid on a HiRISE image of the area. Black dots mark end points of drives, white dots mark significant outcrops, and green lines are 2 m contour intervals. Inset traces the rover traverse from landing to Pahrump Hills. Image credit: Jeffrey Schroeder, NASA, JPL-Caltech, USGS-Flagstaff, University of Arizona. (For interpretation of the references to color in this figure legend, the reader is referred to the web version of this article.)

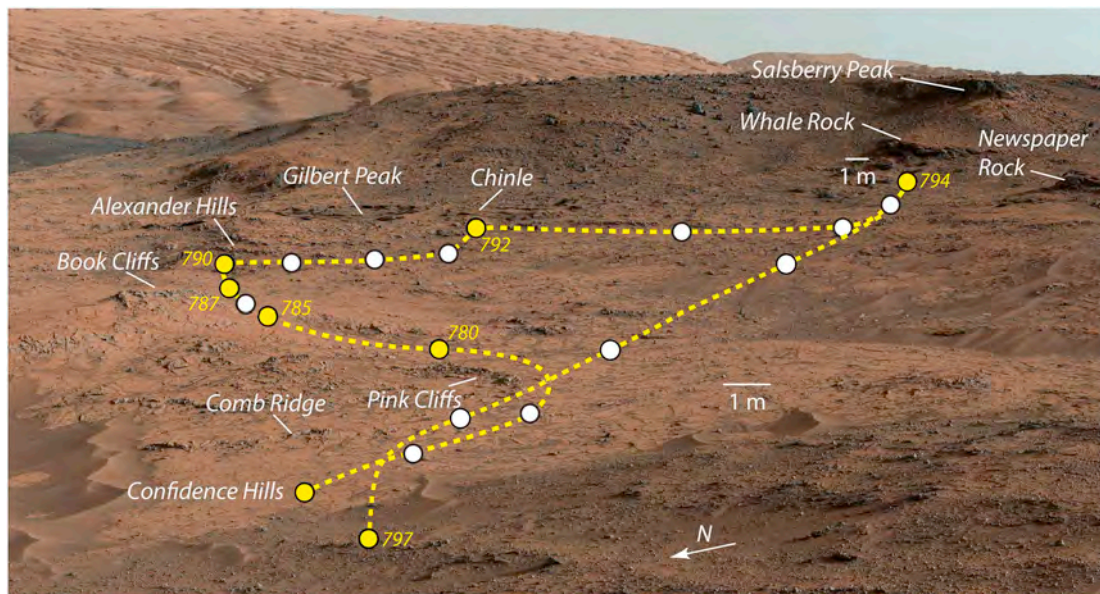


Fig. 2. Mastcam mosaic (mcam03236) of Pahrump Hills with the path taken on the reconnaissance traverse across the outcrop from Sols 780–797. Yellow dashed line marks the traverse path, yellow dots mark end points of drives (waypoints) labeled with the sol of the drive, white dots mark the location of mid-drive imaging by Mastcam. Significant outcrops are identified by name. Different scale bar lengths are due to foreshortening in the mosaic. “Pink Cliffs” is the location of the “Mojave” drilling site; the bedrock below “Whale Rock” is the site of the “Telegraph Peak” drilling site. Mosaic was acquired from the “Sol 751” site in Fig. 1. Modified from JPL Photojournal image PIA19039. (For interpretation of the references to color in this figure legend, the reader is referred to the web version of this article.)

Pahrump Hills outcrop at the “Confidence Hills” site (Sols 753–780), the science team chose to interrogate the geology and chemistry of Pahrump Hills using a “walkabout” strategy (e.g., Arvidson et al., 2014; Yingst et al., 2016a) that began with a reconnaissance traverse around the outcrop to identify and characterize lithologic variability with imaging and chemistry data (Figs. 1 and 2).

The findings from the reconnaissance traverse guided the subsequent contact science traverse to study the sedimentary structures, grain sizes, diagenetic features and chemical characteristics of a subset of the lithologies (Grotzinger et al., 2015; Kah et al., 2018; Nachon et al., 2016; Stack et al., 2019). These observations provided the context for the acquisition of two additional drill samples (“Mojave” and “Telegraph Peak”) (Hurowitz et al., 2017; Martin et al., 2017; Rampe et al., 2017) during the sampling traverse. The collective observations support the hypothesis that the strata exposed at Pahrump Hills represent fine-grained, lacustrine rocks deposited at the distal end of a fluvial-lacustrine system originating from the north rim of Gale crater (Grotzinger et al., 2015; Rivera-Hernández et al., 2017; Stack et al., 2019). Different interpretations exist regarding details of lake chemistry (e.g., Hurowitz et al., 2017; Rampe et al., 2017), lake level fluctuations (e.g., Schieber et al., 2015; Yawar et al., 2018), and sediment sources (e.g., Stack et al., 2018; Williams et al., 2018; Yingst et al., 2016b).

Observations from the entire payload contributed to the interpretation of the Pahrump Hills as a lacustrine deposit, including the Mars Descent Imager (MARDI). MARDI, a nadir-pointed camera, was nominally included on MSL to localize the landing site within Gale crater during descent to the Martian surface. At Pahrump Hills, however, MARDI acquired a continuous record of the Pahrump Hills outcrop as the rover conducted the reconnaissance traverse. MARDI accomplished this task by using the “sidewalk” imaging mode, which acquires images at a constant rate during a rover drive. These images allowed the compilation of a long mosaic of overlapping images that capture, in high detail, the terrain covered by the rover traverse. The mosaic serves as a systematic stratigraphic log of the generally recessive outcrop of the Pahrump Hills, which could not otherwise be obtained by another camera in the payload due to limitations on time, data volume and complexity. This use of MARDI demonstrates that while the camera was designed for one specific use, it could be repurposed to further the scientific return of the mission. Here we show how this repurposing of MARDI, and the resultant continuity and coverage afforded by the MARDI sidewalk mosaic, can be used to systematically identify and characterize features within the outcrop, and to document their spatial distribution and variability in order to gain a broader perspective for understanding the processes that produced them.

2. Investigation and techniques

2.1. MARDI investigation

MARDI is a color, fixed focal length, nadir-pointed camera mounted underneath the front port side of the MSL rover (Malin et al., 2017). The camera head is mounted so that the short axis of the 1600 × 1200 pixel Bayer pattern CCD (7.4 μm square pixels) is parallel to rover motion (when driving straight forward or backward). The primary goal of the MARDI investigation was to locate the exact rover landing site and place that site within the context of local geology imaged during the final ~9 km of the descent and landing of MSL (on August 6, 2012 (UTC) (Vasavada et al., 2014)). Thus, the camera was designed to yield in-focus images from working distances of 2 m to infinity. MARDI includes 8 Gb of flash memory capable of storing 4000 raw images, independent of the rover’s memory.

Although not a primary goal of the investigation, MARDI began regularly acquiring images of the surface beneath the rover on Sol 21. Because the camera is ~66 cm above the surface, MARDI images of the surface are slightly out of focus. Nonetheless, MARDI still resolves mm-scale features over a 92 cm by 64 cm footprint.

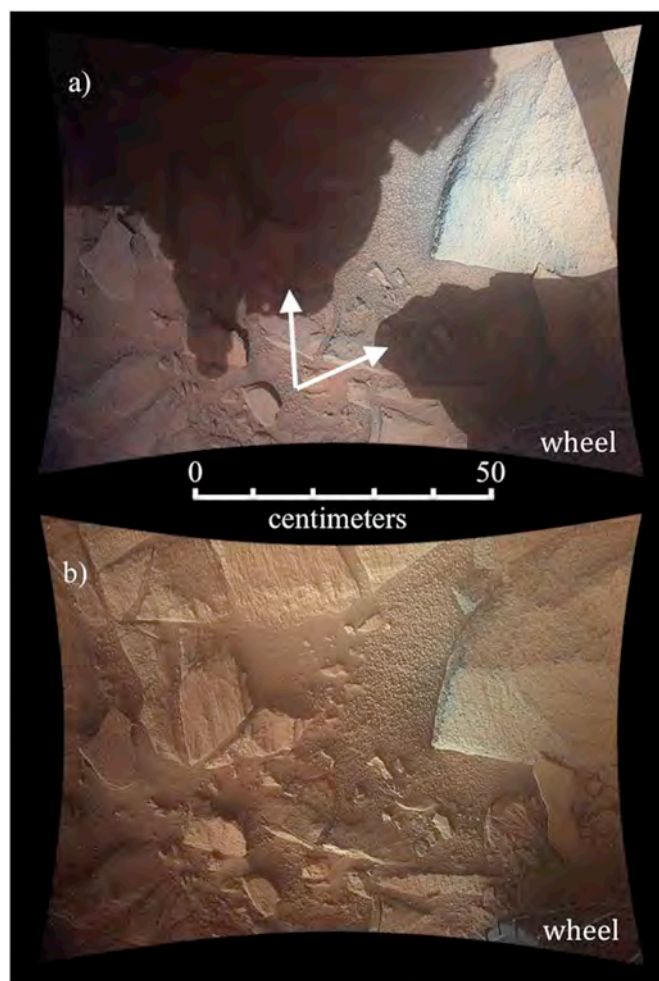


Fig. 3. MARDI images acquired at the same location but at different times of day demonstrate differences in image clarity between direct and diffuse illumination. Location of the wheel is noted in both images. a) Directly-illuminated surface (14:19 LTST, 0739MD0003140010102462M01). Arrows mark the locations of rover-casted shadows within the scene. b) Diffusely-illuminated surface (18:27 LTST, 0739MD0003130000102463E01).

The position of the camera head and its field of view (~70° by 52°) are such that the left front wheel of the rover is visible within most MARDI images (Fig. 3). Dust deposited on the front lens element during landing leads to undesirable scattering when the camera images bright, directly illuminated surfaces (Fig. 3a). For this reason, when possible, MARDI acquires images under indirect or diffuse illumination, typically at twilight (30–45 min after sunset) (Fig. 3b). Imaging at twilight also eliminates illumination extremes (directly illuminated surfaces vs. rover-shadowed surfaces) in a single image, which are greater than the dynamic range of the camera system can effectively capture.

A series of processing steps are then used to correct raw MARDI images. Images are decompressed and expanded to 16 bits, radiometrically processed to remove dark current, corrected for flat field, cross linear filtered to reduce the Bayer pattern noise, then filtered using Adobe Photoshop™ Unsharp Mask (amount = 150%, radius = 1.5 pixels, threshold = 0). The last step enhances features and brings back some fraction of the Bayer pattern noise; thus, the cross linear filter and Unsharp Mask filter steps are repeated. Finally, images are geometrically linearized to compensate for lens distortion. White balancing and gray balancing (using the rover wheel as a gray “standard”) improve the color of MARDI images.

2.2. Sidewalk mode description

MARDI “sidewalk” imaging mode yields a continuous set of images during a rover drive. In this mode, MARDI acquires images at a constant rate (one image every three seconds), but onboard software only saves an image if it is significantly different from the previous image; that is, the Mean-Squared-Error relative to the previous image is larger than a threshold value (Malin et al., 2017). The threshold value can be adjusted and was initially determined from images taken on Earth in the rover testbed. In practice on Mars, this technique leads to at least 75% overlap between consecutive MARDI images along the traverse. All MARDI images saved during a sidewalk imaging activity are stored in MARDI’s internal flash memory. Small, reduced resolution versions of each image (thumbnails; Malin et al., 2017) are downlinked initially, and review of these thumbnails determines which of the images from a given drive will be transmitted to Earth in full resolution. Because of the significant overlap of the sidewalk images, a complete drive path mosaic can be generated using just every third frame of a sidewalk. This reduces the downlink data volume necessary to create a complete sidewalk mosaic. MARDI sidewalks have been acquired at eleven locations since landing, seven of them at Pahrump Hills.

2.3. Sidewalk at Pahrump Hills

During the reconnaissance traverse at Pahrump Hills, sidewalk mosaics were acquired during traverses on Sols 780, 785, 787, 790, 792, 794 and 797. Only on Sol 787 did sidewalk mode fail to yield a continuous record of the drive, for reasons not fully understood, leaving 1–6 m gaps in the mosaic. The total length of the reconnaissance traverse was 152.5 m, and spanned elevations between –4459 m and –4455 m (Table 1). The drive path largely followed the recessive bedrock that dominates at Pahrump Hills (Figs. 1 and 2). On most traverses the rover drove forward, but on all or part of the Sol 794 and 797 traverses, the rover drove backward (Table 1). MARDI acquired 1181 images across the full traverse, and 898 of those images have been downlinked to Earth as lossy JPEGs (compression quality 85; Malin et al., 2017). A mosaic of the complete reconnaissance traverse (Fig. 4) was created from ~500 geometrically corrected full frame images using the open source software Hugin (<http://hugin.sourceforge.net>).

3. Comparison to Mastcam workspace and mid-drive mosaics

The MSL Mastcam instrument consists of two focusable color (Bayer pattern CCD) cameras with different focal lengths, 100 mm (right eye) and 34 mm (left eye), mounted on the remote sensing mast about 2 m above the surface (Malin et al., 2017). The left camera (hereafter referred to as M-34) is focusable from ~2 m to infinity with a 0.22 mrad/pixel image scale, and an $18.4^\circ \times 15^\circ$ FOV (Bell III et al., 2017). M-34 is commonly used to survey rocks, outcrops and geologic context around the rover. During the reconnaissance traverse at Pahrump Hills, M-34 acquired 3×2 workspace mosaics covering ~2 m² in front of the rover after every drive, at scales ranging from ~0.45–0.75 mm/pixel. Before the Sol 780 drive, a larger, 31 image workspace mosaic (with 27 images

subframed to create stereo products with M-100 images) covering ~15 m² was acquired as it was the site of intensive activities associated with drilling at the Confidence Hills location.

During drives on Sols 787, 792, 794 and 797, the rover paused one to four times to acquire 8×1 M-34 mosaics along the starboard side of the rover. These mid-drive mosaics cover ~6 m from the rear right wheel of the rover to ~2 m in front of the front right wheel (Fig. 4). The central 6 frames of each mosaic are sufficiently close to the rover to have pixel scales comparable or better than those of the 3×2 M-34 workspace mosaics (i.e., ≤ 0.75 mm/pixel). The outermost frames achieve pixel scales of ~1 mm/pixel when the rover is on relatively level ground. The M-34 starboard mosaics were another tool employed by the science team to record structures and features within Pahrump Hills, albeit with less coverage than MARDI sidewalk imaging.

The MARDI sidewalk mosaic and M-34 starboard and workspace mosaics overlap in several places along the reconnaissance traverse. The Sol 780 sidewalk intersects the large M-34 workspace mosaic at the Confidence Hills drill site. The first and third M-34 starboard mosaics from the Sol 792 drive overlap the Sol 792 and Sol 794 sidewalk segments, respectively (Fig. 4). The second M-34 starboard mosaic from the Sol 794 drive overlaps the sidewalk from the same drive (Fig. 4). These areas of overlap provide an opportunity to verify how MARDI sidewalk imaging compares to M-34 mosaics with regard to identification and documentation of structures and features along the traverse. M-34 mosaics are used for comparison because the M-34 does not suffer from scattering by dust on the optics, is in full focus, has somewhat better resolution (≤ 0.75 mm/pixel for most of the M-34 starboard and workspace imaging vs. ~1 mm/pixel for MARDI), and typically acquires images of fully illuminated surfaces. The comparisons that follow demonstrate that despite some limitations relative to Mastcam images, the consistent imaging direction, scale, and field of view, and lack of foreshortening of MARDI images make the sidewalk mosaic an effective and, importantly, continuous record of the Pahrump Hills reconnaissance traverse.

Where the Sol 792 sidewalk overlaps the first of three Sol 792 M-34 starboard mosaics (Fig. 5a,b), the MARDI sidewalk records features with comparable fidelity to the M-34. MARDI images with good illumination capture multiple types of features (Section 4) observed at Pahrump Hills: fine (mm-scale) laminae, filled and/or thin-edged fractures, resistant features, and gray clasts strewn on the bedrock surfaces (Fig. 5a). The same features are visible in the M-34 image over the same terrain (Fig. 5b).

An example where MARDI sidewalk imaging underperforms is provided by the overlap between the Sol 794 sidewalk and the third of three Sol 792 M-34 starboard mosaics. Both the almost fully-shadowed MARDI image and the well-illuminated M-34 image exhibit cm-sized, resistant features within the bedrock and gray clasts sitting on the surface of the bedrock (Fig. 5c,d). However, the M-34 image renders laminae that are not visible in the MARDI image, and some resistant features that are apparent in the M-34 image are difficult to discern in the MARDI image. In particular, features located within ~10 cm of the center of the MARDI field of view are more challenging to resolve than those on the edges of the image. The laminae and some fraction of the resistant features might not be identified using the MARDI images alone.

Shadowing is not solely responsible for the poor expression of features in some MARDI sidewalk images, as demonstrated by images from the Confidence Hills drill site. The shadowed Sol 780 sidewalk images capture the features visible in the fully-illuminated M-34 workspace images (e.g., dendritic features, raised edge and filled fractures, gray clasts) with high fidelity (Fig. 5e,f). It is clear from Fig. 5c,d, however, that some combinations of shadowing, overall scene brightness, and location of features within the MARDI field of view can affect the ease of detection of bedrock features in MARDI sidewalk images.

Table 1
Summary of drive characteristics.

Sol	Drive distance (m)	Drive direction	Number of images acquired
780	21.9	Forward	201
785	6.0	Forward	46
787	18.5	Forward	61
790	7.3	Forward	61
792	15.8	Forward	149
794	29.9	Backward (~17.5 m) Forward (~12.4 m)	261
797	53.1	Backward	396

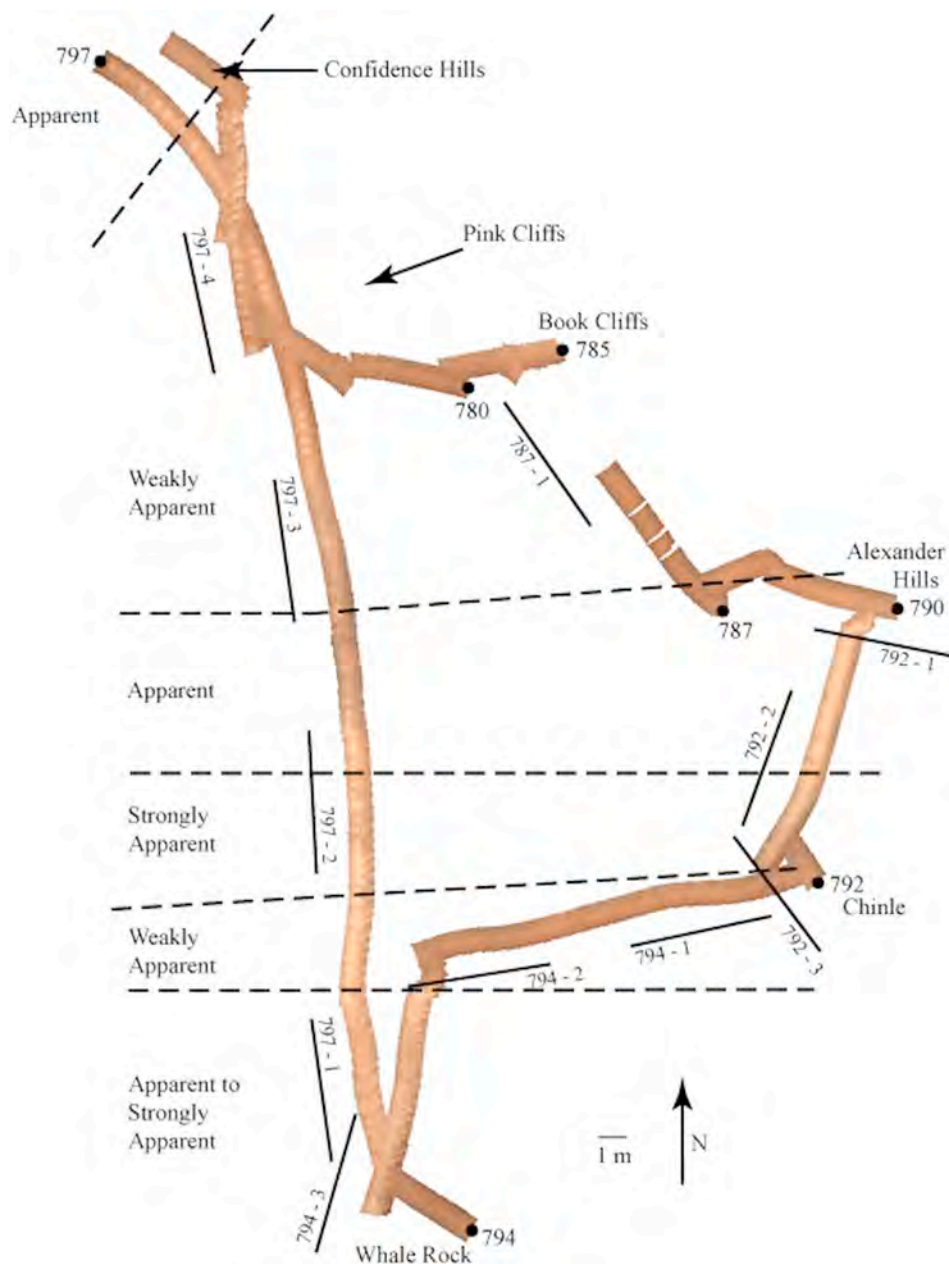


Fig. 4. MARDI sidewalk mosaic over Pahrump Hills. The width of the sidewalk path is the long-axis dimension of a MARDI image (~92 cm). Significant outcrops and waypoints are identified by name; end-of-drive position for each drive sol is identified by a black dot and sol number. Black lines adjacent to the sidewalk mosaic mark locations of ~6 m-long M-34 starboard mosaics; labels indicate their sol of acquisition and the order of acquisition on that sol. Starboard mosaics that fall on the left side of the drive path were acquired when the rover was driving backwards. The root cause of the 1–6 m gaps in the sidewalk between Book Cliffs and Alexander Hills remains undetermined. Spatial distribution of lamination expression is labeled (weakly apparent, apparent, strongly apparent) and delineated by dashed lines (Section 4.1.2).

4. Results

4.1. Laminations

4.1.1. Description of laminae

The recessive mudstone bedrock comprising the dominant lithology at Pahrump Hills (Fig. 2) exhibits thin, regular laminae throughout the outcrop. In MARDI images, the laminae generally appear as mm-spaced stair steps. Laminae are typically parallel to one another and can be traced for distances from a few cm to 80 cm (Fig. 6). Higher resolution imaging of laminae with the Mars Hand Lens Imager (MAHLI, Edgett et al., 2012) places upper limits on the particle sizes of the laminated bedrock. The bedrock matrix material is largely finer than ~62 μm , the smallest particle resolvable at the closest working distance from which MAHLI imaged the bedrock (Grotzinger et al., 2015; Schieber et al., 2015; Schieber, 2018; Stack et al., 2019; Yingst et al., 2017).

The gentle northerly slope of the Pahrump Hills outcrop generally exposes laminae in linear or arcuate forms more or less perpendicular to the outcrop slope (Fig. 6a). Strikes of laminae were measured in at least

one section of each sidewalk drive segment; resulting values range between 50° and 150°. Laminae exhibit an arcuate expression in plan view where they intersect resistant features (Section 4.2) embedded in the outcrop (Fig. 6c).

The appearance, or degree of expression, of the laminae varies across Pahrump Hills, and can be divided into three categories: weakly apparent, apparent and strongly apparent. Weakly apparent laminae are defined by bedrock that shows only isolated patches (10–30 cm^2 in size) of coherent laminae over a span of multiple meters along the sidewalk path (Fig. 6a). Weakly laminated bedrock has a smooth or mottled appearance in the MARDI images. Bedrock with apparent laminae has laminated rock extending for ≥ 1 m along the sidewalk path, and within that span contains coherent, traceable layers 30–40 cm long and generally perpendicular to the drive direction (Fig. 6b). Bedrock with strongly apparent laminae also has laminated rock extending for ≥ 1 m along the sidewalk path and contains consistent, traceable laminae across most to all of the MARDI field of view (Fig. 6c). Strongly apparent laminae tend to be accentuated by the presence of resistant features and their interaction with bedrock topography, and

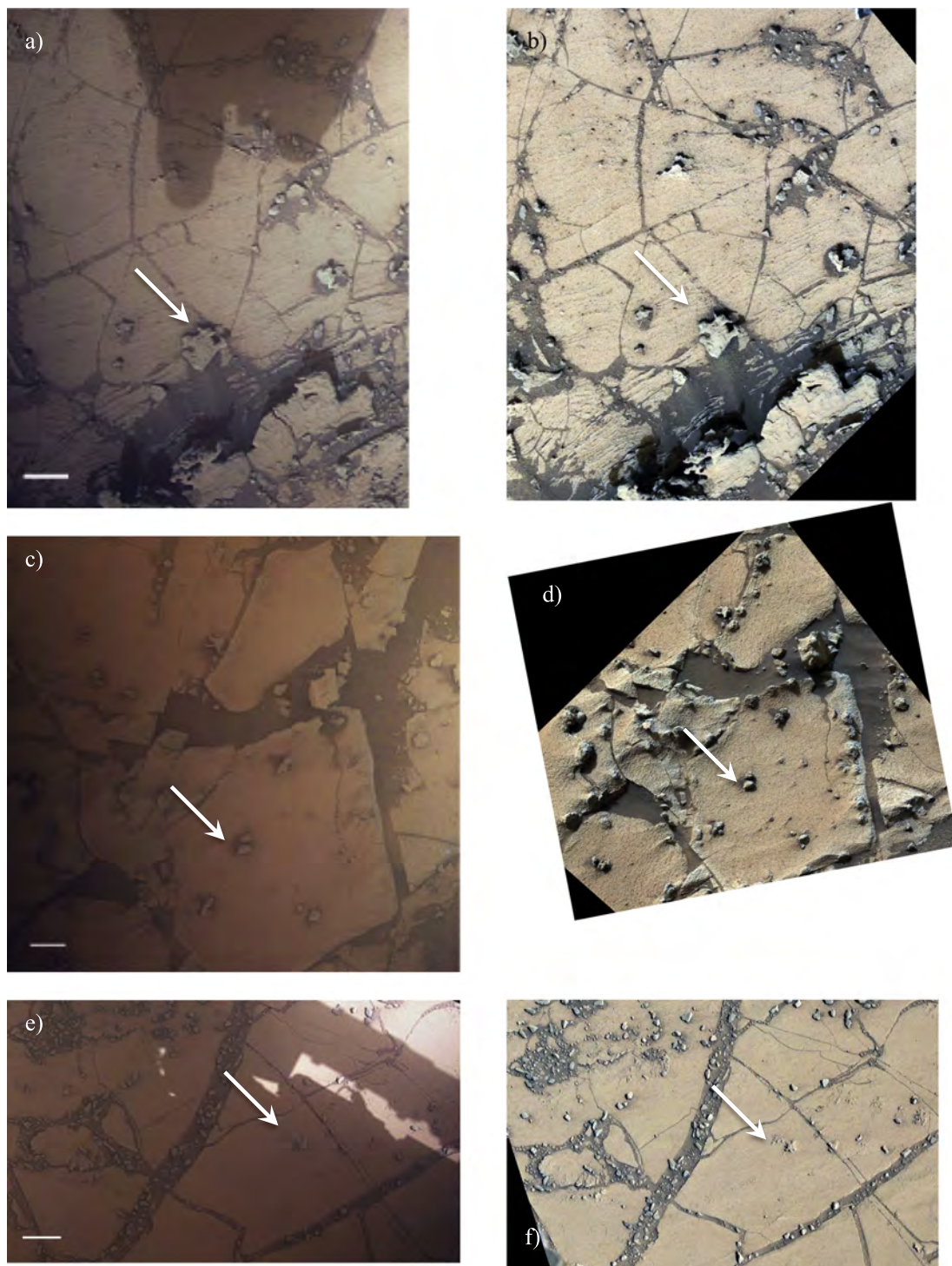


Fig. 5. Comparison of sedimentary structures and resistant features seen in overlapping MARDI sidewalk and M-34 images. White arrows in image pairs point to the same feature in each image. Each Mastcam image is fully illuminated. a) Cropped MARDI image (0792MD0003350010102881M01). Rover shadow impinges on the top center portion of the scene. Scale bar is 5 cm. b) Cropped and rotated M-34 image (0792ML0034530060400564) overlapping a). c) Cropped MARDI image (0794MD0003370010103047M01). Scene is fully shadowed. Image brightness increased 60%. Scale bar is 5 cm. d) Cropped and rotated M-34 image (0792ML0034550020400576) overlapping c). e) Cropped and rotated MARDI image (0780MD0003270010102486M01). Scene is largely shadowed except for portions of the upper right corner. Image brightness increased 20%. Scale bar is 5 cm. f) Cropped and rotated M-34 image (0753ML0032370160400017E01) overlapping e).

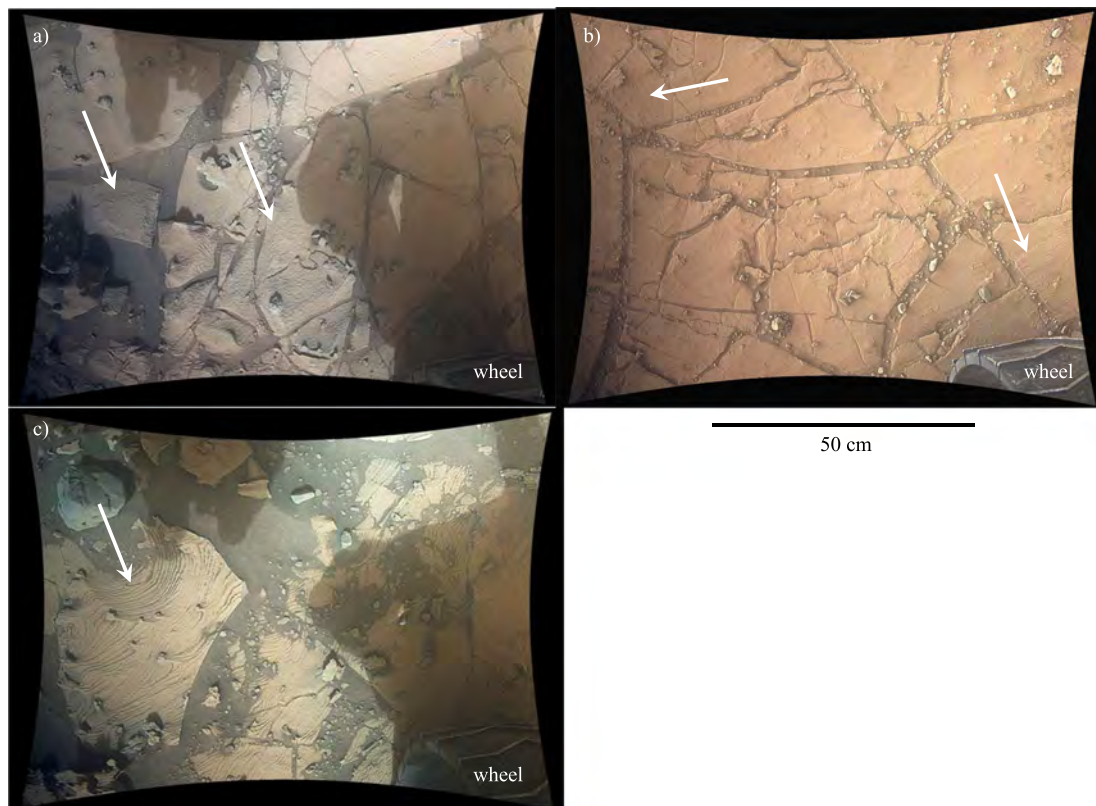


Fig. 6. Laminae in the Pahrump Hills bedrock. Arrows point to type examples in each image.

a) Weakly apparent laminae (Sol 792, 0792MD0003350010102890M01). Rover shadows fall along the top and right portions of the image. b) Apparent laminae (Sol 754, 0754MD0003260000102475E01) in a diffusely-illuminated (no shadows) twilight image. Image brightness increased 20%. c) Strongly apparent laminae (Sol 792, 0792MD0003350010102939M01) where some laminae are exposed by surface topography that cuts into the outcrop slope. Rover shadows fall along the top and right portions of the image.

accumulations of darker sands in the steps between successive laminae.

4.1.2. Distribution of laminae

The spatial distribution of bedrock sections exhibiting weakly apparent, apparent and strongly apparent laminae can be tracked because the sidewalk mosaic traverses up and down outcrop slope, and laterally across the outcrop in two different areas (Figs. 1 and 4). In the northernmost ~2 m of the sidewalk mosaic (collected on Sols 780 and 797; Fig. 4), the bedrock exhibits apparent laminae. Apparent laminae are also known to exist in the Pahrump Hills bedrock to the base of the section (the “Shoemaker” location north of Confidence Hills; Schieber, 2018). As the sidewalk segments (Sols 780, 785, 787, 790 and 797) extend up section (Fig. 2), they exhibit weakly apparent laminae from ~1–2 m south of the Confidence Hills drilling site to roughly the latitude of the “Alexander Hills” waypoint (Fig. 4). The Sol 790 and 797 segments capture the transition from weakly apparent to apparent laminae in this area. Apparent laminae remain the dominant type until ~3–4 m north of the Chinle waypoint, except for 2–4 m-long stretches of weakly apparent laminae visible in the Sol 792 and 797 segments. From this latitude to that of the Chinle waypoint, laminae are strongly apparent in the Sol 792, 794 and 797 segments (Fig. 4). South of Chinle, across the latitude band covered by the segment of the Sol 794 drive that passes E-W across the outcrop (Fig. 4), weakly apparent laminae dominate, but some bedrock slabs up to 70 cm in length are observed to contain apparent laminae. In the Sol 794 and 797 sidewalk segments that lead up section to “Whale Rock”, the southernmost waypoint of the sidewalk (Fig. 4), bedrock becomes increasingly disrupted by both fractures and veins (Section 4.3), and covered by gray clasts (Section 4.4). Together, these features make it challenging to discern laminae in the bedrock slabs. Where bedrock is exposed, however, laminae are

apparent to strongly apparent and in places can be traced across fractures and veins into adjacent bedrock slabs.

4.2. Resistant features

Dendritic features, resistant relative to the surrounding bedrock (Kah et al., 2015; Nachon et al., 2016; Thompson et al., 2015), stood out during initial observations at the Confidence Hills location. In addition, other erosion resistant features with an array of morphologies were observed within bedrock slabs and along bedrock slab margins throughout Pahrump Hills during the reconnaissance traverse. Collectively, these features suggest a prolonged history of diagenetic processes within the Pahrump Hills strata (Kah et al., 2015; Kronyak et al., 2015; Nachon et al., 2016).

4.2.1. Description of resistant features

4.2.1.1. *Compact features.* Compact resistant features occur either embedded within a bedrock slab or along the edges of bedrock slabs. Their morphologies can be broadly categorized as globules, flowers and dendrites. Globules are spherical to sub-spherical in map view and cross section and occur both as individual globules and as groups (Fig. 7a). Their diameters range from 1 to 5 cm. Flowers are roughly spherical to sub-spherical in map view but have gently scalloped edges that impart a lumpier appearance relative to globules (Fig. 7b). Flowers are flatter in cross section than globules. Their diameters range from 0.5 to 5 cm, with most of them falling between 1 and 2 cm in size. Dendrites consist of elongated, finger-like branches that emanate from a central point (Fig. 7c). They have 2–6 branches, with each branch ~0.2–0.4 cm wide and ~0.6–3 cm long. Overall, dendritic features range from ~1.5–4.5 cm in size. There are compact features whose characteristics

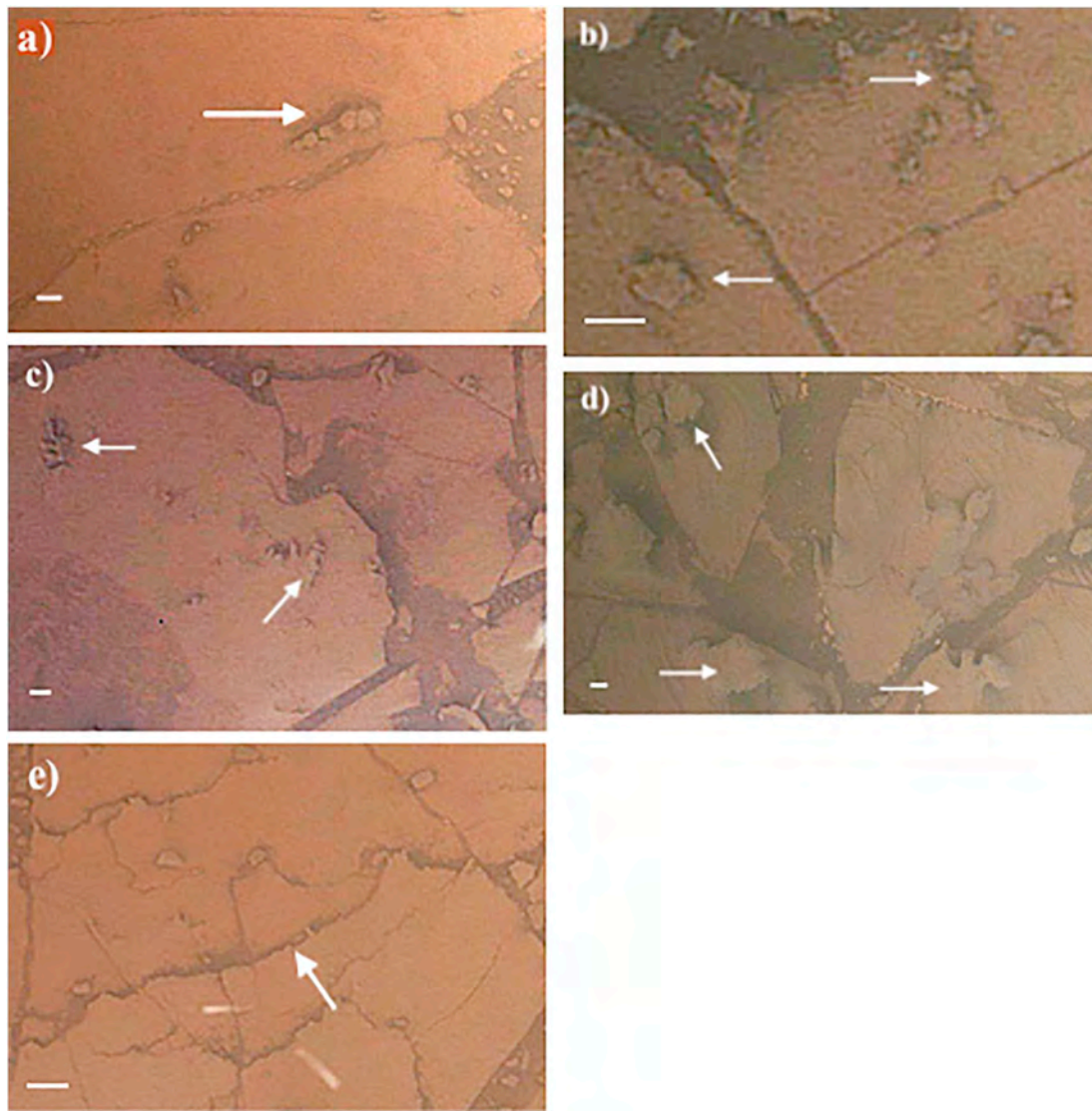


Fig. 7. Resistant feature morphologies seen in the MARDI sidewalk. Arrows in each image point to feature examples. Each image field of view is fully shadowed by the rover. a) Globules (cropped portion of 0785MD0003290010102707M01). Scale bar is 1 cm. Image brightness increased 70%. b) Flowers (cropped portion of 0790MD0003330010102787M01). Scale bar is 2 cm. Image brightness increased 50%. c) Dendrites (cropped portion of 0797MD0003390010103601M01) Scale bar is 1 cm. Image brightness increased 50%. d) Plates (cropped portion of 0790MD0003330010102841M01). Scale bar is 1 cm. Image brightness increased 50%. e) Sheets (cropped portion of 0780MD0003270010102477M01). Scale bar is 2 cm. Image brightness increased 50%.

bridge categories such as spherical globules with irregular protrusions that give them a flower-like appearance, or flowers whose scallops are deeper so as to give them a dendrite-like appearance. Laminae do not show deflections as they intersect resistant features (Fig. 7c).

4.2.1.2. Platy features. Platy features are defined as resistant slabs that protrude from the surrounding bedrock. Morphologies include fans and sheets. Fans occur over a limited lateral distance (~1–6 cm) and have lacy and/or arcuate edges (Fig. 7d). Sheets are thin (≤ 1 cm) and more laterally extensive (~7–30 cm) than fans (Figs. 5a, 7e). Resistant laminae fall under the sheet category, representing the thinnest examples of sheets. They are laminae that are exhumed either around the perimeters of, or within, bedrock slabs. They have lacy, scalloped edges that can have fine (mm-scale) digitate protrusions. In many occurrences, the bedrock surrounding both fans and sheets is eroded sufficiently to leave the fan or sheet suspended above the underlying bedrock.

4.2.2. Distribution of resistant features

Almost every area within the Pahrump Hills sidewalk mosaic exhibits at least one type of resistant feature. The density of features varies throughout the sidewalk mosaic, from low (50–70 features/m²), to moderate (100–200 features/m²), to high (300 or more features/m²). Globules, flowers and fans do not vary in their spatial distribution throughout Pahrump Hills, but dendrites and sheets do. Dendrites are concentrated at the base of the outcrop, particularly near the Confidence Hills drill site, with only rare instances observed south of “Pink Cliffs” (Figs. 1 and 4). Sheets are more prominent in areas of apparent and strongly apparent laminae (Fig. 4).

4.3. Raised edge and filled fractures

The Pahrump Hills outcrop is pervasively fractured, with fractures mm-wide to multiple cm-wide separating the bedrock into polygonal slabs that range in size from a few cm² to ~3.5 m². A subset of these fractures exhibits either erosionally resistant (raised) edges with a

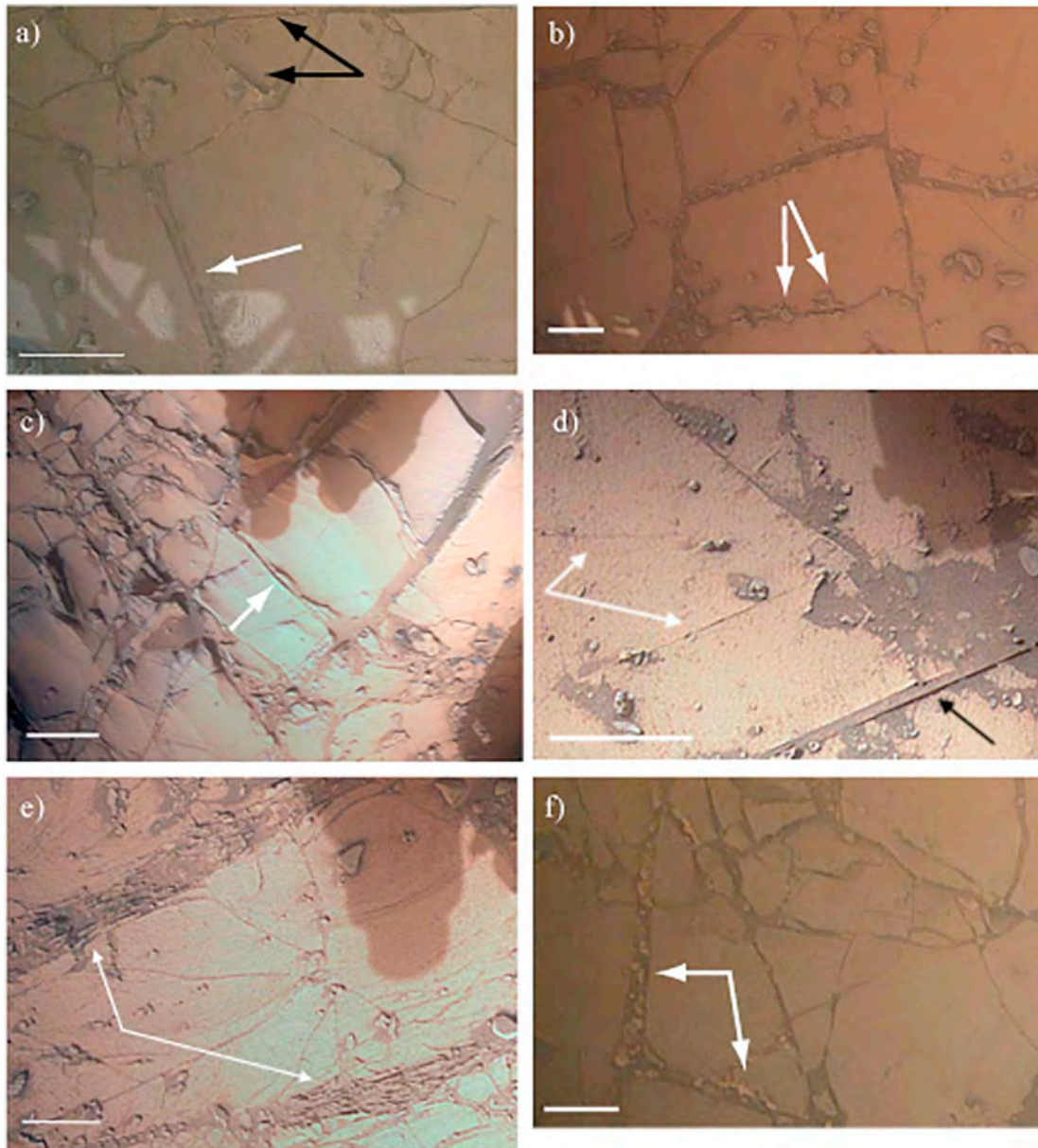


Fig. 8. Fracture morphologies. Rover shadow variably affects each image. a) Fractures with thin raised edges (white arrow) and thin, white fills (black arrows). Cropped portion of 0787MD0003310010102776M01; brightness increased 50%. Scale bar is 10 cm. b) Fracture with resistant features along its edge (white arrows). Cropped portion of 0780MD0003270010102621M01; brightness increased 60%. Scale bar is 5 cm. c) Fractures with tented edges (white arrow). Cropped portion of 0794MD0003370010103152M01. Scale bar is 10 cm. d) Fractures with thin fills (white arrows) and thin raised edges (black arrow). Scale bar is 5 cm. Cropped portion of 0797MD0003390010103426M01. e) Fractures with multilayered fills (white arrows). Cropped portion of 0794MD0003370010103168M01. Scale bar is 5 cm. f) Fractures with irregular white fill (white arrows). Cropped portion of 0790MD0003330010102799M01; brightness increased 50%. Scale bar is 5 cm.

variety of morphologies along the fracture margins or contain fill material (Fig. 8). Raised edges and fill materials are resistant relative to their surrounding bedrock, but are distinguished from other resistant features (Section 4.2) by direct association with a fracture. Individual segments of fractures with raised edges or fills range from 5 to 75 cm in length. Some of these segments belong to single, long fractures that can be traced for distances up to 2 m across bedrock plates.

Fractures with raised edges or with fill materials appear throughout the Pahrump Hills outcrop but the distribution of some types varies locally. Fractures with raised edges and fill materials occur less frequently than resistant features throughout Pahrump Hills.

4.3.1. Description of raised edge and filled fracture morphologies

Raised edge fractures fall into three morphological categories. The

first category consists of fractures with thin (1–2 mm wide) raised edges of uniform relief, which exhibit no deformation of the bedrock adjacent to the fracture edge (Figs. 8a,d). The second category exhibits raised edges of irregular relief imparted by adjacent and/or intersecting resistant features (e.g., dendrites, globules and flowers; Fig. 8) (Fig. 8b). Resistant features along these types of fractures are typically discontinuous, and extend between 5 and 10 mm away from the fracture. Fractures with “tented” edges, the third category, get their appearance when bedrock along the fracture slopes upwards to meet the raised edge of the fracture (Fig. 8c). Widths of tented edges fall between 4 and 10 mm. The bedrock slabs in areas with tented edges tend to an undulating appearance, contrasting with flatter, smoother bedrock slabs elsewhere in the section.

There are also a variety of filled fractures. Thin (1–2 mm wide) filled

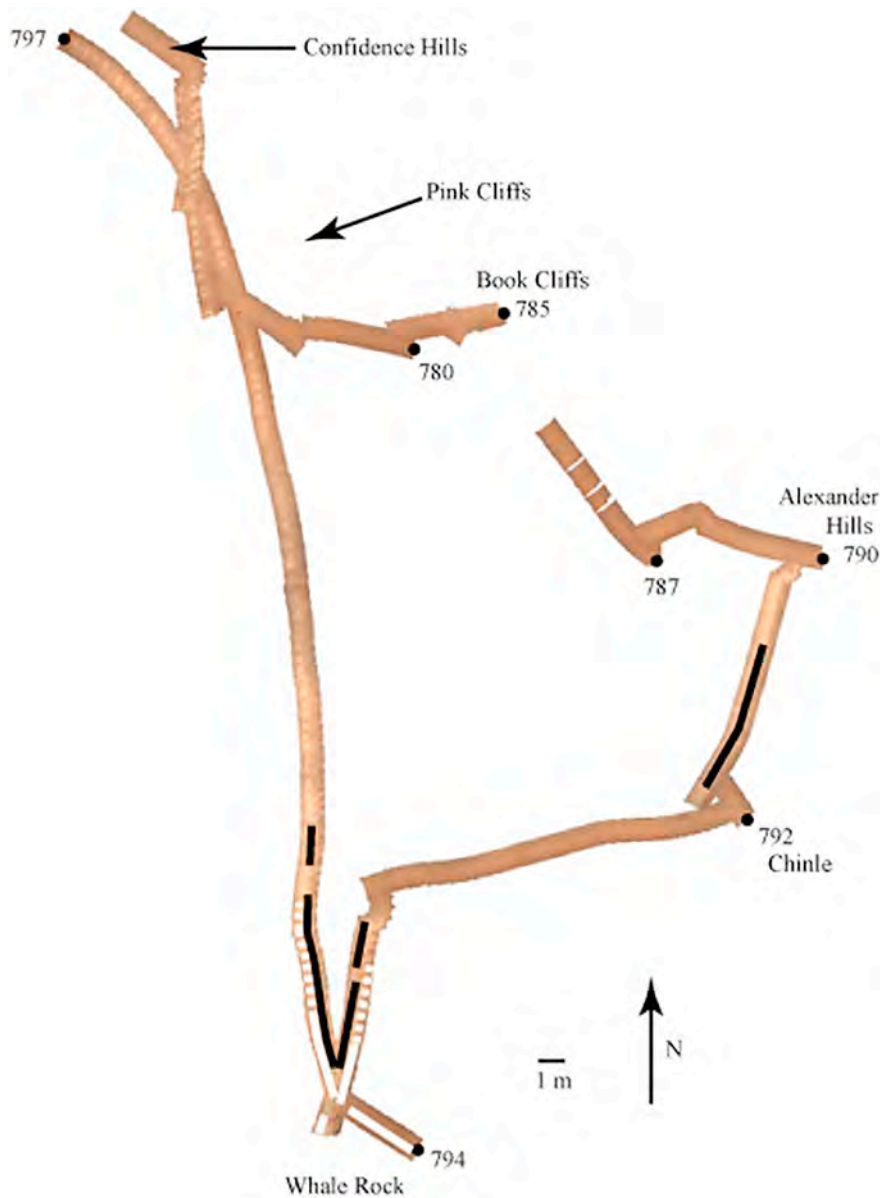


Fig. 9. MARDI sidewalk mosaic over Pahrump Hills. Sol numbers, outcrops, and waypoints labeled as in Fig. 4; Mastcam starboard mosaics are omitted for clarity. Heavy black lines overlying the sidewalk path represent locations of tented fractures. Heavy, solid white lines represent locations of multilayer filled fractures; heavy, dashed white lines represent locations where multilayer filled fractures occur sporadically.

fractures are represented by a single narrow ridge or line of material standing above the bedrock (Fig. 8d). Multilayer filled fractures have overall widths of 2–4 cm and are filled with multiple thin (2 mm), parallel, steeply-dipping layers (Fig. 8e). White filled fractures contain calcium sulfate (Nachon et al., 2014, 2016) and are either thin (2–3 mm) with linear or arcuate shapes (Fig. 8a) or wider (4–15 mm) with irregular fill (Fig. 8f).

Fractures cross cut one another in a variety of relationships. Fractures with resistant features cut those with thin raised edges and vice versa, multilayered fractures cut tented fractures, but most commonly, white filled fractures cut the other fracture types.

4.3.2. Distribution of raised edge and filled fractures

Fractures with fills or raised edges are observed throughout Pahrump Hills with local variations in the type and density of fractures observed. Fractures with thin raised edges and thin fills are present in each sidewalk segment. White-filled fractures are also ubiquitous, but are less common than fractures with thin raised edges and thin fills.

Fractures with resistant features along their edges are most common at the base of the section in the northernmost Sol 780 and 797 drive segments (Figs. 1, 4). Fractures with tented edges are found almost exclusively in two areas: along the Sol 792 drive segment down section (north) from the Chinle waypoint, and from the point where the Sol 794 and 797 segments become parallel (N-S orientation) to where they intersect ~1 m north of Whale Rock (Fig. 9). The lone additional expression of tented fractures is along the Sol 797 drive segment ~1 m north of the E-W segment of the Sol 794 drive (Fig. 9). Multilayer filled fractures begin to appear south of where the Sol 794 and 797 segments become parallel and continue up section toward Whale Rock (Fig. 9); they are not observed anywhere else along the sidewalk path.

4.4. Gray clasts

Gray clasts are loose rock fragments of fine pebble to cobble size (0.4–20 cm longest dimension) with flat faces, smoothed edges, and fine-grained texture (Williams et al., 2006; Yingst et al., 2013, 2016b)

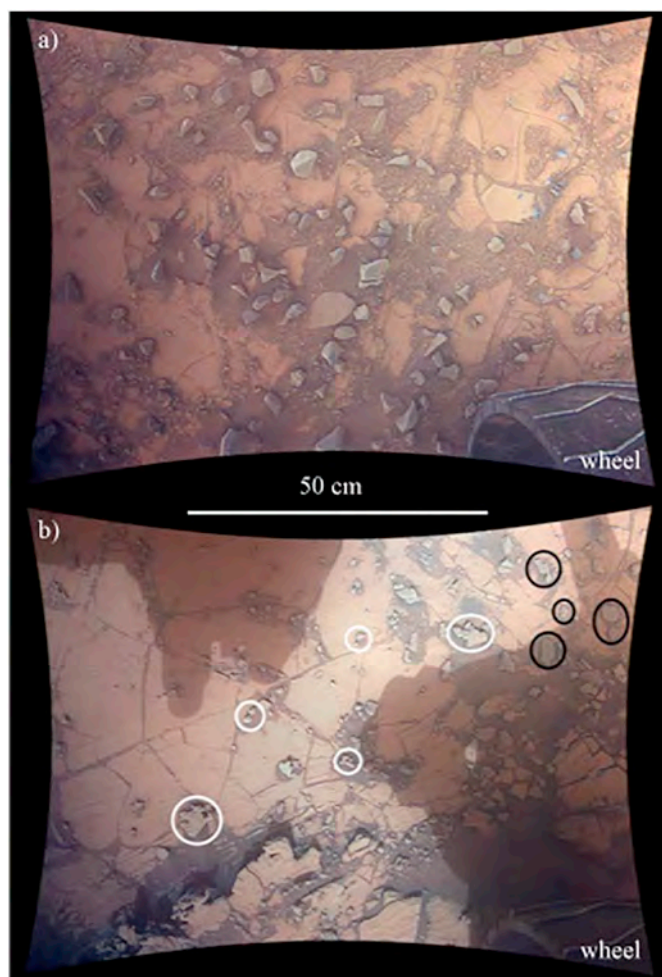


Fig. 10. a) Gray clasts sitting loose over bedrock and fines near the Whale Rock outcrop (0794MD0003380000103260E01) in a diffusely-illuminated (no shadows) image. b) Different rock fragment morphologies present throughout Pahrump Hills (0792MD0003350010102881E01). Black circles enclose examples of gray clasts as in a); white circles enclose examples of rougher, more irregular rock fragments morphologies. Rover-cast shadows partially cover the top and right of the scene in b).

(Fig. 10a). They exhibit a wide variety of shapes including tabular, pyramidal and elongate forms. Gray clasts are observed throughout Pahrump Hills, albeit not uniformly, overlying bedrock and fine-grained soils contained within bedrock fractures. The greatest density and average size of gray clasts is observed along two segments of the Sol 794 drive path: the N-S segment and the segment extending up section to Whale Rock (Figs. 1 and 4). In these segments, densities reach ~ 110 clasts/m², and the average long axis dimension is 3 cm. Elsewhere throughout Pahrump Hills, 0.5–2.6 m long stretches devoid of gray clasts bridge isolated gray clasts or clast patches along the drive paths. Densities in these patches are ≤ 48 clasts/m², and the average long axis dimension is 1–2 cm. Gray clasts are distinguished from other rock fragments observed overlying the bedrock throughout Pahrump Hills which exhibit rougher surface texture, variable color, and irregular shapes (Fig. 10b).

5. Discussion

5.1. Laminations, tented fractures and bedrock slope

The presence of laminations throughout the Pahrump Hills outcrop as revealed by the MARDI sidewalk is consistent with multiple

hypothesized formation scenarios for the recessive mudstone bedrock. Grotzinger et al. (2015) interpret the Pahrump Hills bedrock as a lacustrine deposit that records a cyclic depositional process to form uniform, rhythmic laminations throughout the sequence. Schieber et al. (2015) suggest alternating precipitation and deposition as a source of the laminations, and propose that the laminae reflect alternating wetter and drier intervals, with wetter conditions resulting in the formation of fine-grained (muddy) laminae and drier conditions leading to precipitation of (coarser) evaporite crystals associated with coarser-appearing mudstone laminae. Stack et al. (2019) hypothesize that the laminated mudstone and intermittent, coarser-grained intervals observed at Pahrump Hills were deposited in a lacustrine environment by prograding hyperpycnal plunging river plumes. Coarser-grained intervals are represented by the Chinle (cross stratified mud-siltstone) outcrop, and Whale Rock and Newspaper Rock (cross stratified sandstone) outcrops (Figs. 1 and 2). MARDI does not observe sedimentary structures (e.g., dropstones, mudcracks) that indicate depositional environments for the laminated bedrock (e.g., ice-covered lake, significant dry intervals, aeolian deposition) alternative to the lacustrine formation models. It the context of any of these proposed scenarios it is important to understand how the scenarios might be responsible for the changing expression of laminations (Fig. 4) throughout Pahrump Hills, via breaks in deposition/precipitation, changes in deposition/precipitation mechanisms, variations in grain size, or variations in post-depositional factors such as cementation or alteration.

It is notable that expression of lamination is consistent laterally across Pahrump Hills (Fig. 4), with weakly apparent laminae corresponding to portions of the drive path with smaller differences between end of drive elevations (e.g., Sol 780 to Sol 787). From Confidence Hills to Whale Rock (Figs. 1 and 2), the mudstone bedrock of Pahrump Hills crops out over ~ 7 m in elevation, translating to a regional slope of $\sim 8^\circ$.

To determine whether local variations in slope correlate with variations of lamination expression, we measured terrain slopes along segments of the reconnaissance traverse (Figs. 1 and 2) using the Multi-Mission Geographic Information System tool (MMGIS; Calef et al., 2017) adapted for rover mission operations. The MMGIS tool places engineering data (e.g., rover traverse, planning targets) from *Curiosity* onto orbital images and digital elevation models to enable geographically-localized tracking of the rover drive path and science observations across the terrain. We measured slopes along segments with 2–14 m baselines, which variably corresponded to individual single drives, drive segments (i.e., between turns), or subsets of drive segments (Fig. 11). These measurements show that areas with the steepest slopes ($> 11^\circ$) are areas where strongly apparent laminations are observed, and areas with the smallest slopes ($\sim < 6^\circ$) are areas where laminations are most commonly weakly apparent (Fig. 11). The correlation of lamination expression with slope is not perfect, as weakly apparent and apparent laminations are observed in segments with 6–7° slopes (Fig. 11). Our general observation is that increasing slope correlates with stronger lamination expression. This relationship suggests that laminations are present throughout the Pahrump Hills bedrock, but are better exposed in areas of steeper slopes. The ubiquitous presence of laminated bedrock implies that depositional processes at the lamina scale did not change appreciably during deposition of the mudstone succession at Pahrump Hills.

While depositional processes that resulted in the laminations were consistent, subtle changes in grain size serve as a feasible explanation for elevated slopes, tented fractures and undulating bedrock. Tented fractures and undulating bedrock surfaces are also associated with areas of steeper slopes, and occur down section of the coarser-grained Chinle, Whale Rock and Newspaper Rock horizons (Figs. 9, 11) (Stack et al., 2019). Gradual coarsening of sediment toward these coarse-grained horizons would result in greater permeability and penetration of fluids into the sediment, ultimately resulting in the precipitation of inter-granular cement that has greater resistance to erosion than framework grains. Greater quantities of such cement would create zones around

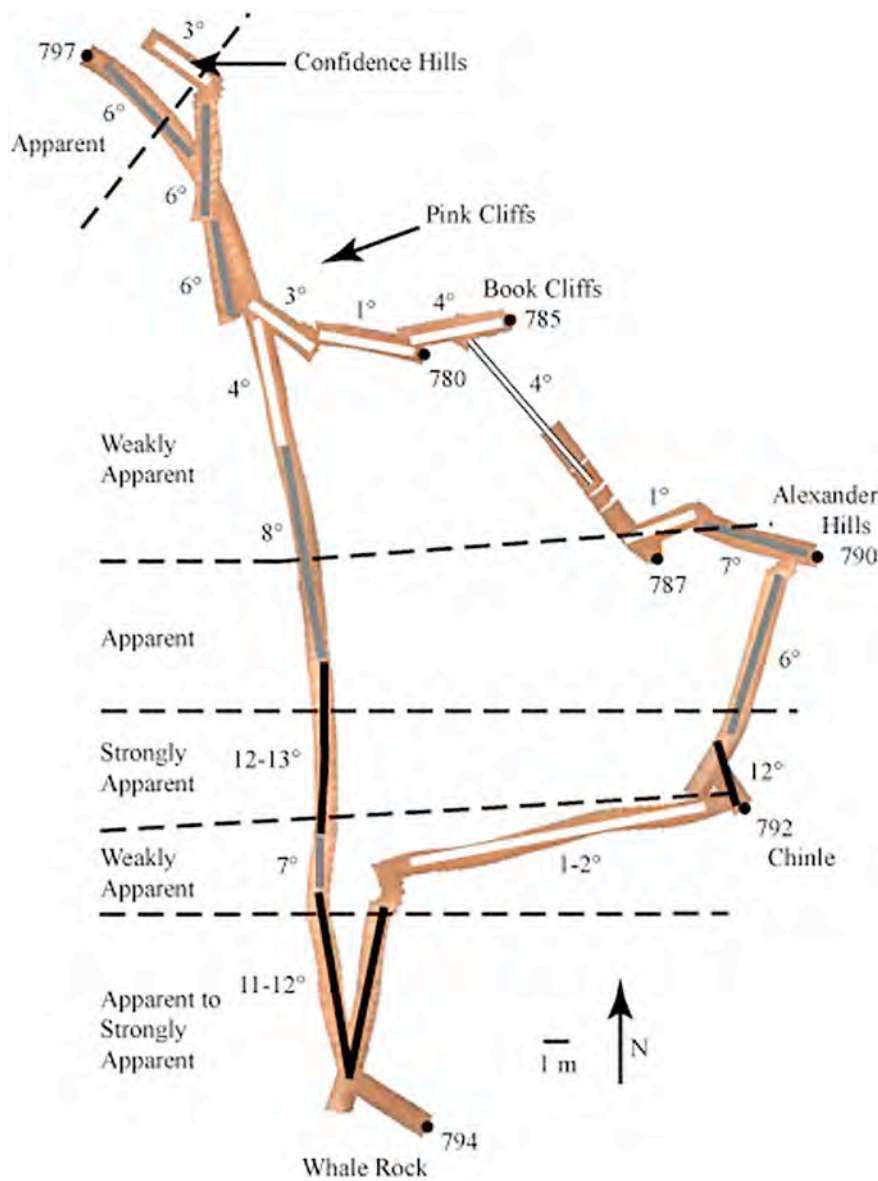


Fig. 11. MARDI sidewalk mosaic over Pahrump Hills. Sol numbers, outcrops, and waypoints labeled as in Fig. 4. Lines overlying the sidewalk mark segments along the drive path where terrain slope was measured. Black solid lines $\geq 10^\circ$; gray solid lines = $6\text{--}8^\circ$; white solid lines $\leq 4^\circ$. Values adjacent to the lines indicate the slope of that segment. Black dashed lines and labels (weakly apparent, apparent, strongly apparent) denoting the spatial distribution of lamination expression as in Fig. 4.

fractures that are more resistant to erosion (tenting fractures) and more resistant bedrock overall (higher slopes exposing laminations more effectively, undulatory bedrock).

The areas of bedrock that exhibit higher slopes correlate well with those areas identified as resistant bedrock by multiple studies (e.g., Mangold et al., 2015; Nachon et al., 2016). They find that the resistant bedrock exhibits elevated amounts of Mg relative to the recessive mudstone bedrock. Specifically, targets at Book Cliffs and Alexander Hills, outcrops that resemble areas with tenting fractures and undulating bedrock surfaces, have higher Mg than recessive bedrock targets like those near Confidence Hills. APXS finds Mg similarly elevated in resistant bedrock relative to recessive bedrock (Thompson et al., 2015). If the areas of greater slope, tenting fractures and undulating bedrock surfaces contain more cement, cement as the Mg carrier could explain the elevated Mg contents of these areas.

5.2. Resistant features

Resistant features observed throughout the MARDI sidewalk are

further evidence of fluid interactions within the Pahrump Hills strata. The morphology of compact and platy resistant features observed by MARDI ranges in size and extent from smaller, simpler forms (e.g., globules) to more complex and laterally extensive forms (e.g., dendrites, sheets). Thus, the morphological spectrum of resistant features reflects localized to expansive cementation and increasing intensity of diagenetic reactions. Underlying controls could be duration of fluid interaction, fluid composition, and permeability of the sediment. The occurrence of resistant features throughout Pahrump Hills indicates a pervasive diagenetic overprint of the sediment package. Further, MARDI images do not show any evidence for laminae deflecting around resistant features (e.g., Fig. 6c) suggesting the diagenetic overprint occurred relatively late in burial history.

MARDI also observed resistant features in the Murray formation, of which the Pahrump Hills is the basal section. Systematic post-drive MARDI imaging recorded characteristics of the Murray formation on a path extending ~ 6 km and climbing ~ 150 m from Pahrump Hills (Miniti et al., 2017). Resistant features of mm- to cm-scale were observed in 90% of the MARDI images along the traverse through the

Murray formation (Minitti et al., 2017). As at Pahrump Hills, the resistant features were not observed to deflect laminations (Minitti et al., 2017). This extends the observations of this study, indicating that an extensive, late diagenetic overprint affected not only Pahrump Hills, but the Murray formation as a whole.

Other studies support conclusions drawn from MARDI observations of resistant features. A variety of studies interpret resistant features as diagenetic in origin (Kah et al., 2015; Nachon et al., 2016; Sun et al., 2018). MAHLI images at Pahrump Hills also indicate that laminations do not show evidence for differential compaction around dendrites (Kah et al., 2015). Kah et al. (2015) suggest that dendrites (e.g., Fig. 7c) and resistant features along fractures (e.g., Fig. 8b) formed during burial diagenesis, with the former nucleating within the sediment and the latter nucleating along fractures that were conduits for mineralizing fluids. Sun et al. (2018) tracked the morphology, size and density of resistant features (interpreted as concretions) throughout the Murray formation using Mastcam and MAHLI imaging. They observe a variety of concretion morphologies (dendrites, spherules, flat, irregular, lamination enhancing), some of which are not observed at Pahrump Hills. Where laminations and concretions coexist, laminae are not deformed around the concretions (Sun et al., 2018).

The elemental chemistries of resistant features at Pahrump Hills provide insight into the origin of elevated Mg contents of resistant (high slope) bedrock. APXS measurements show elevated amounts of Mg, Ni, Br, Cl and S, relative to the recessive host bedrock, in the dendrites near Confidence Hills (Thompson et al., 2015). Mg and S contents are positively correlated, suggesting the presence of a MgSO_4 phase. Ni is positively correlated with Mg and S, suggesting that the Ni is associated with the MgSO_4 phase (Thompson et al., 2015). ChemCam analyses of dendrites corroborate the elevated Mg, Ni and S contents of these features (Nachon et al., 2016). Nachon et al. (2016) also report element enrichments in resistant features like those observed by MARDI. A target that falls in the flower category (Fig. 7b) exhibits Mg enrichment relative to the background bedrock (“Searles”; Nachon et al., 2016). A target that falls in the sheet category (Figs. 5a, 7e) exhibits slight elevations in Mg and S (“Hayden Peak”; Nachon et al., 2016). The presence of elevated Mg in resistant diagenetic features, and in areas of tented fractures and elevated slopes, suggests a genetic link such as a common fluid that caused cementation and alteration of the initial sediment. Thompson et al. (2015) hypothesize that briny fluids could have leached Mg and Ni from the sediment and re-precipitated as Mg and Ni-bearing cements, or that Mg and Ni-rich fluids replaced mineral grains and earlier formed cements.

5.3. Thin raised edge and filled fractures

Fundamental bedrock characteristics, such as grain size differences inferred from the tented fractures, may also help explain the thin raised edge and thin filled fractures observed throughout Pahrump Hills. Rather than coarser grain sizes (and an accompanying increase in permeability) yielding tented fractures, finer grain sizes (with decreased permeability) could hinder the penetration of fluids into the bedrock, and thus limit mineral precipitation to within open fractures. The recessive mudstone bedrock that dominates Pahrump Hills (and the terrain covered by the MARDI sidewalk) is fine grained (e.g., mudstone to very fine sand; Rivera-Hernández et al., 2017; Stack et al., 2019; Yingst et al., 2017). This is consistent with the presence of thin filled and thin raised edge fractures throughout this recessive bedrock.

There is only a single ChemCam analysis of a target that falls under the thin raised edge category of this work (“Castlegate_2”; Nachon et al., 2016). This target exhibits Na and Fe enrichments relative to the background bedrock, but no Mg enrichment as observed in the resistant features or the bedrock resembling the tented fractures (Nachon et al., 2016). The thin filled fractures of this study were not analyzed for chemistry. However, a portion of MAHLI images acquired during the contact science and sampling traverses at Pahrump Hills capture

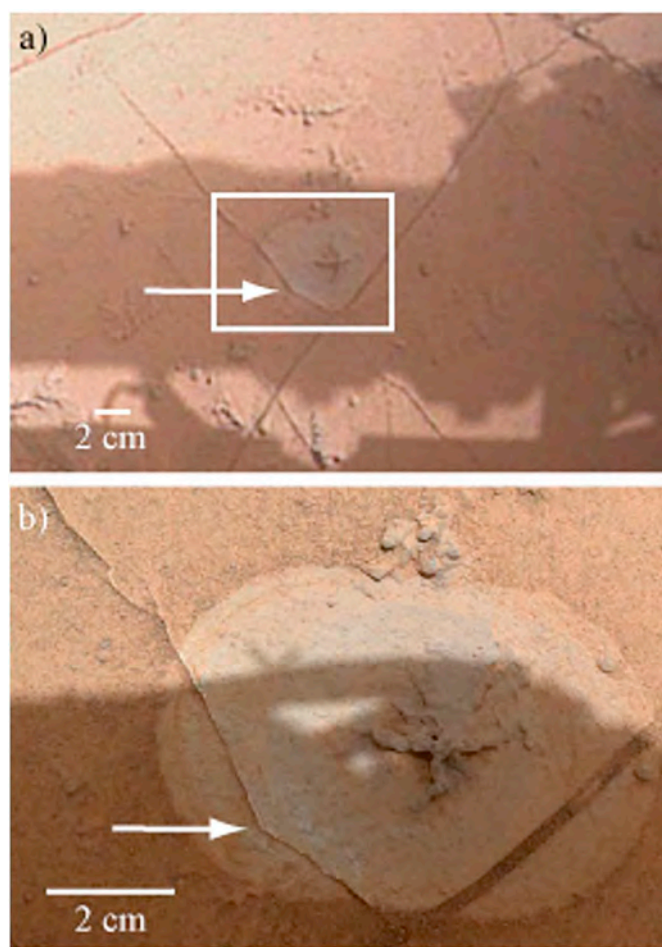


Fig. 12. Two views of a thin filled fracture. a) Cropped MARDI image (0780MD0003270010102489M01) exhibiting a thin filled fracture (white arrow) that cuts through a brushed (dust-removed) spot over the “Morrison” dendritic resistant feature. White box delineates the field of view of b). Rover shadows cut laterally across the image. b) Cropped and rotated MAHLI image (0767MH0001900010300135C00) of the scene within the white box in a). Both inside and outside the brushed area, the white color of the thin fracture fill is apparent. Rover shadow darkens the bottom half of the image.

examples of thin filled fractures that provide insight into their composition (Fig. 12). In these examples, the fill within thin filled fractures is white (Fig. 12), linking them to the wider white filled fractures observed throughout Pahrump Hills (Fig. 8a,f). Multiple white filled fractures were measured at Pahrump Hills (Nachon et al., 2016), and their calcium sulfate chemistry ties them to white filled fractures observed throughout Gale crater (Kronyak et al., 2015; Nachon et al., 2014; Schieber et al., 2017). The presence of calcium sulfate veins along *Curiosity's* entire traverse, through hundreds of meters of stratigraphy, speaks to a larger (and later) fluid fracturing event that broadly impacted the sediments of Gale crater after deposition (e.g., Kronyak et al., 2015; Nachon et al., 2014).

Multilayer filled fractures occur in a restricted area (Fig. 9), suggesting a unique set of conditions for their formation. If each layer formed in the same way that a thin fill or thin raised edge formed (i.e., a discrete episode of fluid flow and mineral precipitation), multiple layers would suggest reutilization of a single parent fracture. Kronyak et al. (2019) observe multi-phase fracture fills indicative of the reutilization of pre-existing fractures, which is consistent with MARDI observations. Compositional data were not acquired from any multilayer filled fracture examples observed within the Pahrump Hills.

The variety of observed fracture fill morphologies and chemistries

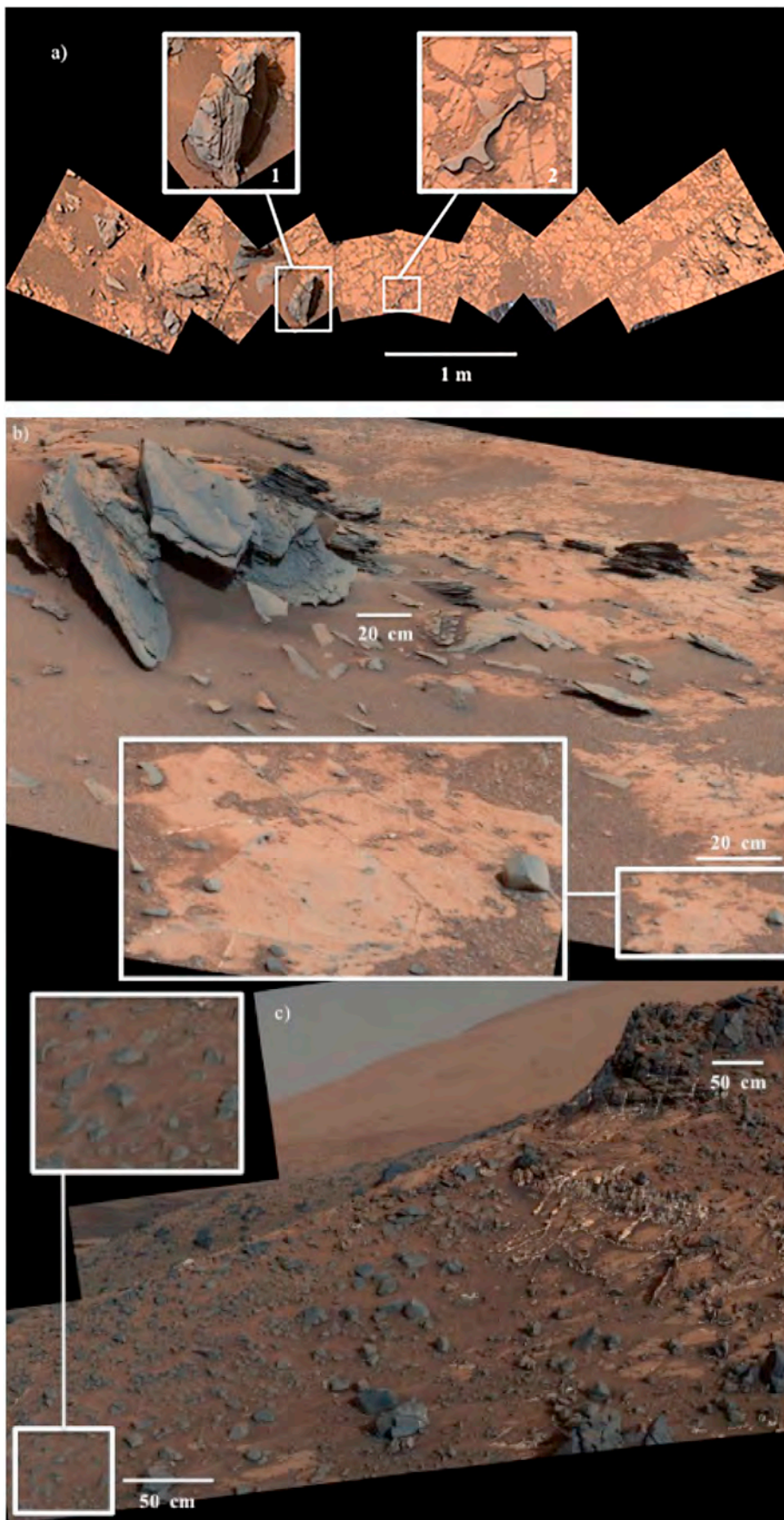


Fig. 13. a) Vertically-projected M-34 starboard mosaic (mcam03485) acquired during the Sol 797 drive (797-1, Fig. 4) exhibiting large blocks eroded from the Whale Rock outcrop. Inset 1 focuses on a block from the Whale Rock outcrop and Inset 2 focuses on tabular and arcuate gray clasts that have the same character as the layers within the Whale Rock block. b) M-100 mosaic (mcam04040) covering part of the Newspaper Rock outcrop (Fig. 2). Inset focuses on tabular and more equant gray clasts in proximity to, and thus plausibly derived from, the outcrop. c) M-100 mosaic (mcam04119) of a portion of the Salberry Peak outcrop (Fig. 2) and the scree slope at its base. Inset exhibits tabular, arcuate and more equant gray clasts shed from the outcrop.



Fig. 14. M-34 image (0792ML0034550030400577C00) exhibiting rock fragments that originated as resistant features within the Pahrump Hills bedrock. White circles enclose in-place resistant features; yellow circles enclose examples of rock fragments with textures and sizes comparable to resistant features. (For interpretation of the references to color in this figure legend, the reader is referred to the web version of this article.)

suggests a complex history of fracturing and fluid interaction within the strata exposed at Pahrump Hills. The fracture fill observations can be explained with an overall model that begins with fluid-induced fracturing of the entire Pahrump Hills section after deposition, consolidation, and burial. Fluids then interact with the wall rock of these fractures and surrounding bedrock as dictated by local grain size and permeability. Given the cross cutting relationships among the fracture types, it appears that multiple fracturing events occurred, each with a unique fluid chemistry that left behind distinct chemistry. At least three types of fluids are required to yield the fracture fill chemistries (Mg-enriched, Na- and Fe-enriched, Ca-sulfate; Nachon et al., 2014, 2016) observed throughout Pahrump Hills.

5.4. Gray clasts

Gray clasts strongly resemble fragments eroded from the sandstone horizons at Whale Rock, Newspaper Rock, and Salsberry Peak (Figs. 2, 10a, 13). Gray clasts with tabular and arcuate forms and which expose stratification are most easily connected to the flat slabs eroded from the cross-stratified Whale Rock and Newspaper Rock outcrops (Figs. 13a,b); the more pyramidal forms may have been sourced from either Whale Rock/Newspaper Rock or Salsberry Peak outcrops (Fig. 13). Higher density of gray clasts and a greater average long axis at the south end of Pahrump Hills is consistent with derivation from Whale Rock, Newspaper Rock and/or Salsberry Peak. However, gray clasts are found throughout Pahrump Hills and not just at the southern (up section) end. The gray clasts found far from Whale Rock, Newspaper Rock and Salsberry Peak could have been derived from stratigraphic equivalents of these sand deposits that were present in the since-eroded volume above Pahrump Hills. Alternatively or additionally, multiple observations support sediment transport from the south (Gale crater interior) as contributing to the strata observed by *Curiosity* (e.g., Stack et al., 2018; Williams et al., 2018; Yingst et al., 2016a, 2016b). Thus, the gray clasts could also record sediment from a different lacustrine period or depositional system within Gale crater.

Gray clasts are distinguished from other rock fragments found throughout Pahrump Hills that are of variable colors, have rougher

textures, and have irregular shapes (Fig. 10b). MARDI and Mastcam images demonstrate that these other fragments originated from multiple sources including resistant features, tented fracture areas or coarser-grained bedrock horizons (e.g., Pink Cliffs, Alexander Hills) throughout the Pahrump Hills exposure (Figs. 10b, 14).

Gray clasts like those observed throughout Pahrump Hills are not common in MARDI images of the Murray formation. Systematic post-drive MARDI imaging of the Murray formation (Minitti et al., 2017) identified gray clasts comparable to those at Pahrump Hills (e.g., gray, smooth, rounded edges, tabular and pyramidal shapes) near “Marias Pass” (Sols 1031–1071), “Ireson Hill” (Sols 1597–1608), and six stops in between. These gray clast occurrences have significantly smaller spatial densities and tend to have smaller sizes than those at Pahrump Hills. A complex interplay of surface erosion mechanisms and rates for both the mudstone substrate and the overlying sandstones is likely required to explain the distribution of gray clasts like those found at Pahrump Hills throughout the rest of the Murray formation.

6. Conclusions

The MARDI sidewalk mosaic serves as an effective tool for systematic mapping of primary and secondary sedimentary features throughout the Pahrump Hills outcrop traversed by the *Curiosity* rover. The following conclusions were enabled by the continuity and coverage afforded by the MARDI sidewalk mosaic:

Lamination of the recessive mudstone bedrock is pervasive, with variations in the degree of lamination expression observed throughout Pahrump Hills. Degree of expression correlates with local bedrock slopes, with low slopes associated with weakly apparent laminations and high slopes associated with strongly apparent laminations. Laminae throughout the bedrock indicate that processes at the lamina scale did not change appreciably during deposition of the mudstone succession at Pahrump Hills.

Resistant features observed throughout Pahrump Hills include compact and platy morphologies. Resistant features do not deflect laminae around them, suggesting they formed comparatively late in burial history. The consistent presence of resistant features throughout Pahrump Hills is evidence that the diagenetic overprint associated with their formation was pervasive. The range of observed features, from simpler, more compact forms to larger, more complex forms, may reflect localized to expansive cementation and increasing intensity of diagenetic reactions.

Fractures cut the Pahrump Hills bedrock and exhibit a variety of fill and raised edge morphologies. Thin fill and thin raised edge fractures are indicative of less fluid penetration into the bedrock, whereas tented fractures are indicative of greater fluid penetration. White fracture fills contain calcium sulfate, tying these particular Pahrump Hills fractures to sulfate fracture fills observed throughout the entire *Curiosity* rover traverse (e.g., Nachon et al., 2014; Kronyak et al., 2015; Minitti et al., 2017).

Multilayered fractures, found exclusively in the southern section of Pahrump Hills near Whale Rock, appear to have formed by multiple episodes of fracturing and filling.

Smooth gray clasts are found consistently throughout Pahrump Hills, sitting loosely on the recessive outcrop and intervening fines. Their color, shape and texture are consistent with derivation from Whale Rock, Newspaper Rock and/or Salsberry Peak, including both the present-day outcrops and their (now eroded) equivalents that would have sat stratigraphically above the present-day recessive mudstone bedrock.

Acknowledgements

This research was supported by NASA with contracts through the Jet Propulsion Laboratory to Malin Space Science Systems (1516826) and through Malin Space Science Systems to MEM (#17-0468). The

authors wish to thank the Mars Science Laboratory engineering, operations and science teams for their combined efforts toward the continuing success of the mission. MEM wishes to thank two reviewers for their constructive comments and suggestions. All data used are available through the Planetary Data System.

References

- Anderson, R.B., Bell III, J.F., 2010. Geologic mapping and characterization of Gale crater and implications for its potential as a Mars Science Laboratory landing site. *Mars* 5, 76–128.
- Arvidson, R.E., et al., 2014. Ancient aqueous environments at Endeavour crater, Mars. *Science* 343 no. 6169. <https://doi.org/10.1126/science.1248097>.
- Bell III, J.F., et al., 2017. The Mars science laboratory curiosity rover mast camera (Mastcam) instruments: pre-flight and in-flight calibration, validation, and data archiving. *Earth Space Sci.* 4, 396–452. <https://doi.org/10.1002/2016EA000219>.
- Calef III, F.J., Abarca, H.E., Soliman, T., Abercrombie, S.P., Powell, M.W., 2017. Multi-Mission geographic information system for science operations: a test case using MSL data. *Planetary Data Workshop 3* (Abstract #7111).
- Edgett, K.S., et al., 2012. Curiosity's Mars Hand Lens Imager (MAHLI) investigation. *Space Sci. Rev.* 170, 259–317. <https://doi.org/10.1007/s11214-012-9910-4>.
- Grotzinger, J.P., et al., 2012. Mars Science Laboratory Mission and science investigation. *Space Sci. Rev.* 170, 5–56. <https://doi.org/10.1007/s11214-012-9892-2>.
- Grotzinger, J.P., et al., 2015. Deposition, exhumation, and paleoclimate of an ancient lake deposit. *Gale crater, Mars. Science.* <https://doi.org/10.1126/science.aac7575>.
- Hurowitz, J.A., et al., 2017. Redox stratification of an ancient lake in Gale crater, Mars. *Science* 356. <https://doi.org/10.1126/science.aah6849>.
- Kah, L.C., Kronyak, R.E., Van Beek, J.K., Nachon, M., Mangold, N., Thompson, L., Wiens, R.C., Grotzinger, J.P., Farmer, J., Miniti, M.E., Schieber, J., Oehler, D., 2015. Diagenetic crystal clusters and dendrites, lower Mount Sharp, Gale crater. *Lunar Planet. Sci. Conf.* 46 (Abstract #1901).
- Kah, L.C., Stack, K.M., Eigenbrode, J.L., Yingst, R.A., Edgett, K.S., 2018. Syndepositional precipitation of calcium sulfate in Gale Crater, Mars. *Terra Nova* 30, 431–439. <https://doi.org/10.1111/ter.12359>.
- Kronyak, R.E., Kah, L.C., Nachon, M., Mangold, N., Wiens, R.C., Williams, R.M.E., Schieber, J., Grotzinger, J.P., 2015. Distribution of mineralized veins from Yellowknife Bay to Mount Sharp, Gale crater, Mars: insight from textural and compositional variation. In: *Lunar Planet. Sci. Conf.* vol. 46 (Abstract #1903).
- Kronyak, R.E., Kah, L.C., Edgett, K.S., VanBommel, S.J., Thompson, L.M., Wiens, R.C., et al., 2019. Mineral-filled fractures as indicators of multigenerational fluid flow in the Pahrump Hills member of the Murray formation, Gale crater, Mars. *Earth and Space Science* 6, 238–265. <https://doi.org/10.1029/2018EA000482>.
- Malin, M.C., et al., 2017. The Mars Science Laboratory (MSL) Mast Cameras and Descent Imager: I. Investigation and instrument descriptions. *Earth and Space Science* 4 (8), 506–539. <https://doi.org/10.1002/2016EA000252>.
- Mangold, N., Forni, O., Blaney, D.L., Milliken, R., Nachon, M., Le Deit, L., Gasnault, O., Clegg, S., Fisk, M., Grotzinger, J., Hurowitz, J., Kah, L.C., Le Mouélic, S., McLennan, S., Maurice, S., Stack, K., Sumner, D.Y., Wiens, R.C., the MSL Team, 2015. ChemCam analyses of the Pahrump Hills sediments in the context of other sediments analysed by the curiosity rover. In: *European Planetary Science Congress.* vol. 10 (EPSC2015-102).
- Martin, P.E., Farley, K.A., Baker, M.B., Malespin, C.A., Schwenzer, S.P., Cohen, B.A., Mahaffy, P.R., McAdam, A.C., Ming, D.W., Vasconcelos, P.M., Navarro-González, R., 2017. A two-step K-Ar experiment on Mars: dating the diagenetic formation of jarosite from Amazonian groundwaters. *J. Geophys. Res. - Planets* 122 (12), 2803–2818. <https://doi.org/10.1002/2017JE005445>.
- Milliken, R.E., Grotzinger, J.P., Thomson, B.J., 2010. Paleoclimate of Mars as captured by the stratigraphic record in Gale Crater. *Geophys. Res. Lett.* 37, L04201. <https://doi.org/10.1029/2009GL041870>.
- Miniti, M.E., Kennedy, M.R., Krezoski, G.M., Rowland, S.K., Schieber, J., Stack, K.M., Yingst, R.A., 2017. Using MARDI twilight images to assess variations in the Murray formation with elevation, Gale crater, Mars. In: *Lunar Planet. Sci. Conf.* vol. 48 (Abstract #2622).
- Nachon, M., et al., 2014. Calcium sulfate veins characterized by ChemCam/Curiosity at Gale crater, Mars. *J. Geophys. Res. Planets* 119. <https://doi.org/10.1002/2013>.
- Nachon, M., et al., 2016. Chemistry of diagenetic features analyzed by ChemCam at Pahrump Hills, Gale crater, Mars. *Icarus.* <https://doi.org/10.1016/j.icarus.2016.08.026>.
- Rampe, E.B., et al., 2017. Mineralogy of an ancient lacustrine mudstone succession from the Murray formation, Gale crater, Mars. *Earth Planet. Sci. Letts.* 471, 172–185. <https://doi.org/10.1016/j.epsl.2017.04.021>.
- Rivera-Hernández, Frances, Dawn, Y., Mangold, Nicolas, Stack, Kathryn M., Forni, Olivier, Newsom, Horton, Williams, Amy, Nachon, Marion, L'Haridon, Jonas, Gasnault, Olivier, Wiens, Roger, Maurice, Sylvestre, 2019. Using ChemCam LIBS data to constrain grain size in rocks on Mars: Proof of concept and application to rocks at Yellowknife Bay and Pahrump Hills, Gale crater. *Icarus* 321 (2019), 82–98. <https://doi.org/10.1016/j.icarus.2018.10.023>.
- Schieber, J., 2018. How small is it? Pushing MAHLI to the limit in the search for mudstones at Gale crater, Mars. *Lunar Planet. Sci. Conf.* 49 (abstract #1100).
- Schieber, J., Sumner, D., Bish, D., Stack, K., Miniti, M., Yingst, A., Edgett, K., Malin, M., Grotzinger, J., the MSL science team, 2015. The Pahrump succession in Gale crater — A potential evaporite bearing lacustrine mudstone with resemblance to earth analogs. *Lunar Planet. Sci. Conf.* 46 (Abstract #2153).
- Schieber, J., Bish, D., Coleman, M., Reed, M., Hausrath, E.M., Cosgrove, J., Gupta, S., Miniti, M.E., Edgett, K.S., Malin, M., 2017. Encounters with an uneartly mudstone: understanding the first mudstone found on Mars. *Sedimentology* 64, 311–358. <https://doi.org/10.1111/sed.12318>.
- Stack, K.M., Williams, R.M.E., Grotzinger, J.P., Rubin, D.M., Frydenvang, J., Seeger, C.H., 2018. Sandstones and conglomerates at the foothills of mount sharp, Gale crater, Mars: Facies analysis and stratigraphic implications. In: *Lunar Planet. Sci. Conf.* vol. 49 (Abstract #1712).
- Stack, K.M., Grotzinger, J.P., Lamb, M.P., Gupta, S., Rubin, D.M., Kah, L.C., Edgar, L.A., Fey, D.M., Hurowitz, J.A., McBride, M., Rivera-Hernández, F., Sumner, D.Y., Van Beek, J.K., Williams, R.M., Aileen Yingst, R., 2019. Evidence for plunging river plume deposits in the Pahrump Hills member of the Murray formation, Gale crater, Mars. *Sedimentology.* <https://doi.org/10.1111/sed.12558>.
- Sun, V.Z., Stack, K.M., Kah, L.C., Thompson, L., Fischer, W., Williams, A.J., Johnson, S.S., Wiens, R.C., Kronyak, R.E., Nachon, M., House, C.H., VanBommel, S., 2018. Late-stage diagenetic concretions in the Murray Formation, Gale Crater, Mars. *Icarus* 321. <https://doi.org/10.1016/j.icarus.2018.12.030>.
- Thompson, L.M., Gellert, R., Spray, J.G., Kah, L.C., APXS team, the MSL team, 2015. The composition of the basal Murray formation at Pahrump Hills, Gale crater, Mars. In: *Lunar Planet. Sci. Conf.* vol. 46 (Abstract #1429).
- Thomson, B.J., et al., 2011. Constraints on the origin and evolution of the layered mound in Gale crater, Mars, using Mars Reconnaissance Orbiter data. *Icarus* 214, 413–432. <https://doi.org/10.1016/j.icarus.2011.05.002>.
- Vasavada, A.R., Grotzinger, J.P., Arvidson, R.E., Calef, F.J., Crisp, J.A., Gupta, S., Hurowitz, J., Mangold, N., Maurice, S., Schmidt, M.E., Wiens, R.C., Williams, R.M.E., Yingst, R.A., 2014. Overview of the Mars Science Laboratory mission: Bradbury Landing to Yellowknife Bay and beyond. *J. Geophys. Res. Planets* 119, 1134–1161. <https://doi.org/10.1002/2014JE004622>.
- Williams, J., Arsenaault, M.A., Buczkowski, B.J., Reid, J.A., Flocks, J.G., Kulp, M.A., Penland, S., Jenkins, C.J., 2006. Surficial sediment character of the Louisiana offshore continental shelf region: A GIS compilation. In: *United States Geological Survey Open-File Report 2006–1195*.
- Williams, R.M.E., Malin, M.C., Stack, K.M., Rubin, D.M., 2018. Assessment of Aeolis Palus stratigraphic relationships based on bench-forming strata in the Kylie and the Kimberley regions of Gale crater, Mars. *Icarus* 309, 84–104. <https://doi.org/10.1016/j.icarus.2018.02.028>.
- Yawar, Z., Schieber, J., Miniti, M., Van Beek, J., Calef, F., Edgett, K., Malin, M., 2018. With the nose to the ground – exploring the Pahrump Hills outcrop with MARDI for new perspectives on the mudstones of the Murray formation at Gale crater, Mars. *Lunar Planet. Sci. Conf.* 49 (Abstract #1101).
- Yingst, R.A., et al., 2013. Characteristics of pebble and cobble-sized clasts along the Curiosity rover traverse from Bradbury landing to Rocknest. *J. Geophys. Res. Planets* 118 (11), 2361–2380. <https://doi.org/10.1002/2013JE004435>.
- Yingst, R.A., Berger, J., Cohen, B.A., Hynes, B., Schmidt, M., 2016a. Determining best practices in reconnoitering sites for habitability potential on Mars using a semi-autonomous rover: a GeoHeuristic Operational Strategies Test. *Acta Astron* 132, 268–281. <https://doi.org/10.1016/j.actaastro.2016.12.018>.
- Yingst, R.A., Cropper, K., Gupta, S., Kah, L.C., Williams, R.M.E., Blank, J., Calef III, F., Hamilton, V.E., Lewis, K., Shechet, J., McBride, M., Bridges, N., Martinez Frias, J., Newsom, H., 2016b. Characteristics of pebble and cobble-sized clasts along the Curiosity rover traverse from sol 100 to 750: terrain types, potential sources, and transport mechanisms. *Icarus* 280, 72–92. <https://doi.org/10.1016/j.icarus.2016.03.001>.
- Yingst, R.A., Kah, L., Stack Morgan, K., Edgett, K., McBride, M., Harker, D., Herkenhoff, K., Miniti, M., Rowland, S., 2017. Textures of rocks at Pahrump Hills, Gale crater, Mars, as revealed by the Mars Hand Lens Imager. *EGU* 19, 9702.